Near-field optical imaging and spectroscopy of a coupled quantum wire-dot structure

Valentina Emiliani,* Francesca Intonti, Christoph Lienau, and Thomas Elsaesser
Max-Born-Institute für Nichtlinear Optic und Kurzzeitspektroskopie, Max-Born-Str. 2a, D-12489 Berlin, Germany

Richard Nötzel and Klaus H. Ploog
Paul-Drude-Institute für Festkörperelektronik Hausvogteiplatz 5-7, D-10117 Berlin, Germany

(Received 17 April 2001; published 20 September 2001)

A coupled GaAs/AlGaAs quantum wire (QWR)-dot sample grown by molecular beam epitaxy on a patterned (311)*A* GaAs substrate is studied by near-field spectroscopy at a temperature of 10 K with a spectral resolution of 100 μeV. The two-dimensional potential energy profiles of the sample including localized excitonic states caused by structural disorder are determined in photoluminescence measurements with a spatial resolution of 150 nm. One finds a potential barrier of 20 meV between the quantum wire and the embedding quantum well (QW) on the mesa top of the structure. This is due to local thinning of the GaAs layer. In contrast, the wire-dot interface results free of energy barriers. The spatial variation of the GaAs layer thickness provides information on the growth mechanism determined by lateral diffusion of Ga atoms which is modeled by an analytical model. By performing spatially resolved photoluminescence excitation measurements on this wire-dot structure, we present a method for investigating carrier transport in low-dimensional systems: The dot area is used as an optical marker for excitonic diffusion via QW and QWR states. The two-dimensional (2D) and 1D diffusion coefficients are extracted as a function of the temperature and discussed.

DOI: 10.1103/PhysRevB.64.155316 PACS number(s): 78.67.−n

I. INTRODUCTION

The electronic and optical properties of low-dimensional semiconductor nanostructures are determined by the quantum-mechanical confinement of electronic wave functions which results from a spatial variation of the band structure of the material on a nanometer length scale. Realization of quasi-one-dimensional (1D) and zero-dimensional confinement, i.e., of quantum wires (QWR's) and quantum dots (QD's), is based on epitaxial growth of layered structures in which a controlled variation of material composition and/or thickness as well as self-organized growth mechanisms lead to quantum confinement. Scanning probe techniques such as atomic force microscopy, scanning tunneling microscopy and related techniques play an important role for the *structural* characterization of such nanostructures with atomic resolution and enable the study of *single* nanostructures. Optical spectroscopy with subwavelength spatial resolution, e.g., confocal and near-field scanning optical microscopy (NSOM), allow one to address single nanostructures and to study their electronic properties. Both single quantum wires[1–6] and quantum dots[7–11] have been investigated in steady-state experiments. The recent successful combination of NSOM with time resolved techniques has opened the possibility to image carrier dynamics in single nanostructures by performing space *and* time resolved experiments.[12–16]

The optical properties of QWR's are determined by quasi-one-dimensional quantum confinement and by disorder-induced fluctuations of the confinement potential.[5] Both spatially extended quasi-1D excitonic states and excitons localized in disorder-induced QD-like potential minima contribute to the overall luminescence spectrum, as was demonstrated recently for a GaAs/AlGaAs QWR structure grown by molecular beam epitaxy on a patterned (311)*A* GaAs substrate.[17] In growing such structures, disorder is difficult to control and, thus, a random spatial distribution of localized QD-like states occurs. For studying coupling mechanisms between different types of low-dimensional states, e.g., 1D and 0D states, structures with a well-defined spatial arrangement of QWR and QD are essential. In this paper, we study the optical properties of a GaAs/AlGaAs nanostructure on a patterned (311)*A* GaAs substrate in which dotlike areas are intentionally introduced at the intersection of adjacent QWR segments. We map the local confinement potentials by photoluminescence NSOM and demonstrate distinctly different optical transition energies of the dot area and the QWR segments. The absence of a potential barrier between QWR segments and dot area allows the dot to be used as a local optical marker for carrier transport along the QWR. Diffusive exciton transport is directly imaged, providing quantitative information on diffusion coefficients.

The paper is organized as follows. In Sec. II, the sample structure and the experimental setup are described. In Sec. III, we present the optical characterization of the structure. This section is divided in four parts.

(i) Overview of the optical properties of the sample: The luminescence properties of QW, QWRs and dots are spatially and spectrally resolved.

(ii) Investigation of growth dynamics: Starting from the near-field PL optical images, a 2D topography of the structure with the single monolayer precision is derived. The results of an analytical model for explaining the self-ordering of the quantum nanostructures are successfully compared with the experimental findings.

(iii) Characterization of the wire-dot interface: The optical map of the sample allows one to establish that such a structure is suitable for transport experiment providing evidence for electronic coupling between the wire and the dot region.

In Sec. IV, spatially resolved PLE measurements are performed in order to optically investigate exciton transport properties in a single QWR: Through the variation of the distance between excitation spot and dot, detailed insight

 ©2001 The American Physical Society

into the drift-diffusive motion of excitons within the embedding QW and along the QWR are obtained. 2D and 1D diffusion coefficients are extracted from the spatial profile of the PLE images along the QW and the QWR directions, respectively. Conclusions are presented in Sec. V.

II. EXPERIMENTAL

The GaAs/(AlGa)As nanostructure is grown by MBE on patterned GaAs(311)A substrates. In such structures, QWRs are formed due to the preferential migration of Ga ad-atoms from the mesa top and bottom towards one of the sidewalls of mesa stripes oriented along [01-1].[18] The combination of this growth mechanism with appropriate lithographic patterning of the sample surface allows the controlled fabrication of novel nanostructures.[19] In particular, a quantum wire-dot structure has been realized by growth of a zig-zag pattern with sidewalls alternatingly misaligned by $+$ or $-30°$ from [01-1].[20] The inset in Fig. 1 (a) shows a schematic top view of the structure. The sample consists of a nominally 3 nm thick GaAs QW layer clad between 50 nm $Al_{0.5}Ga_{0.5}As$ barriers. The upper barrier is covered by a 20 nm GaAs protective layer.

Spatially resolved near-field spectroscopic experiments were performed at temperatures between 10 and 300 K, with a home-built near field optical microscope.[21] For the optical characterization of the sample the microscope is used in the illumination/collection geometry: the excitation laser (photon energy 1.96 eV) is transmitted through the near-field fiber tip and the PL emitted from the sample is collected through the same fiber. High-energy resolution images are recorded by acquiring PL spectra at each tip position with a $f=50$ cm monochromator in conjunction with a liquid-nitrogen cooled back-illuminated charge-coupled-device (CCD) camera. We achieve a combined spatial and spectral resolution of 150 nm and 100 μeV, respectively.

For the optical transport measurements, the microscope is used in the illumination geometry. A tunable narrow-band Ti:sapphire laser (bandwidth $\leqslant 200$ μeV) is coupled into the fiber tip for the excitation. The PL emission from the sample is collected in far-field through a conventional microscope objective, dispersed in a 0.25-m double monochromator with a spectral resolution of 1.2 meV and detected with a silicon avalanche photodiode. Spatially resolved images are recorded by scanning the probe tip over the sample.

Near-field fiber probes are made by chemically etching single mode optical fibers.[22] They are used in the illumination/collection mode without metal coating. When used in the illumination mode, the tips are coated with a 50–100 nm thick aluminum layer.

III. RESULTS: LOCAL OPTICAL PROPERTIES, POTENTIAL PROFILES AND GROWTH MECHANISM

A. Local optical properties

An overview far field PL spectrum [Fig. 1(a)] is recorded with the tip positioned near the corner of the intersection of two inclined sidewalls and collecting the PL signal through a microscope objective. Three major emission peaks at 1.64, 1.67, and 1.72 eV and a weak shoulder at 1.74 eV are visible. Their spatial origin is revealed by the two-dimensional (2D) near-field images shown in Fig. 1(b). The emission at the lowest energy (1.64 eV) originates from the corners of the two intersecting sidewalls that point toward the mesa top. At these positions dotlike regions are formed. For detection at 1.67 eV we find a homogeneous QWR emission along the entire length of the zig-zag sidewalls, interrupted around the position where the first image reveals dot formation. The PL at 1.72 eV extends on both mesa top and bottom and originates from exciton recombination in the flat QW area. The last image shows the spatial distribution of the PL signal at 1.74 eV (the weak shoulder). This emission region is located between the QWR (dark area in the upper part of the image) and the mesa top. The photon energy from this region is higher than both the QW and the QWR emissions, i.e., represents an energy *barrier* between the mesa top and the QWR.[12,23]

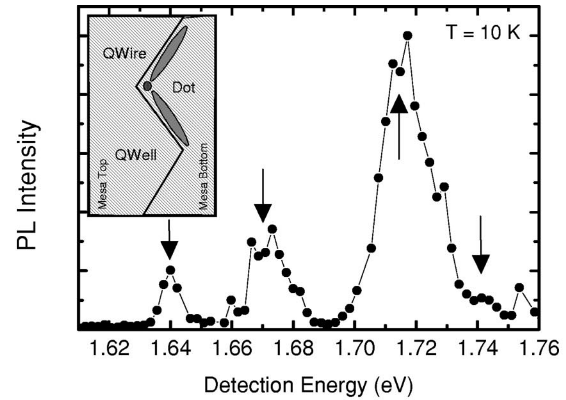

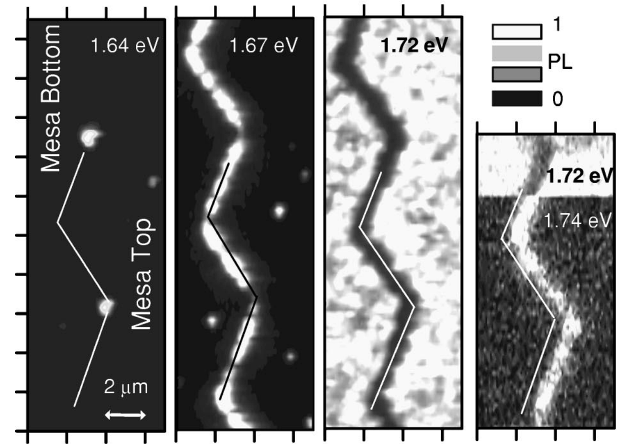

FIG. 1. (a) Far-field photoluminescence spectrum ($T=10$ K) of the coupled wire-dot structure recorded with a spatial resolution of 3 μm by positioning the tip at the corner of the sidewall intersection. The arrows indicate the energies of the three main recombination peaks and the energy of the shoulder used as detection energies for the images in Fig. 1(b); Inset: schematic of the structure. (b) Normalized near-field PL images recorded at the detection energies indicated in the figure and by arrows in Fig. 1(a). Excitation with HeNe laser (1.96 eV)

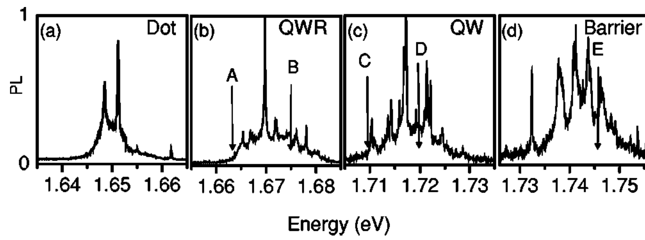

FIG. 2. High-resolution near-field PL spectra recorded at (a) the dot, (b) wire, (c) well, and (d) barrier positions; $T=10$ K, excitation energy=1.96 eV, excitation density=10^{10} cm^{-2}. The arrows indicate the detection energy selected for the 2D images of Fig. 3. For each spectrum the signal is normalized to the maximum PL.

In order to extract more details from the optical map, high spectral—and spatial—resolution images were recorded around the dot by restricting the scan region to an area of 4×5 μm^2 with a pixel of 100 nm. For this set of data PL spectra were recorded in the illumination/collection geometry as described in Sec. II.

Near-field spectra recorded with the tip located at the dot, wire and well positions are shown in Figs. 2(a)–2(c). The emission band centered at 1.74 eV is also clearly resolved [Fig. 2(d)]. All the spectra show a set of sharp and intense emission peaks with spectral widths that range from 100 to 350 μeV. These sharp peaks are superimposed on broad background emissions. 2D near-field images, recorded at the spectral position of the sharp lines show that these PL contributions stem from regions resolution limited in size.[17] Thus, they are attributed to the emission from excitons localized at local minima of the disordered nanostructure potentials. These fluctuations arise from a local roughness of the interface layers as well as from alloy fluctuations in the barrier layers.[10]

Most of the sharp emission spikes originate from excitons localized in spatially distinct 0D islands. This is clearly resolved in our experiments, as the *two-dimensional* spatial variations of the emission intensity from two spectrally distinct sharp spikes are clearly different even if the spatial separation of the corresponding 0D islands is less than the spatial resolution of our experiment. In general, the spectral fluctuations of the individual sharp emission lines bear only little direct information about the statistical parameters—namely, the correlation length[24,25]—of the disoder potential that governs exciton localization in these nanostructures. We have recently demonstrated[24] that such information can indeed be very precisely obtained from a statistical analysis of the two-energy autocorrelation of such near-field spectra. A detailed comparison of this autocorrelation function with a quantum theory of the exciton center-of-mass motion in a two-dimensional spatially correlated disorder potential allows one to extract a correlation length of about 17 nm and a disorder strength of 5 meV for the quantum well region of our sample. This analysis also gives clear evidence for a quantum-mechanical repulsion of exciton levels in the disordered quantum well and allows one to estimate the localization length of the exciton wave function. When the detection energy is tuned out of the sharp spectral and spatial resonances, a completely different spatial variation of the PL behavior is revealed. This is shown in Fig. 3, where we select PL images at the representative energies indicated by arrows in Fig. 2. Both in the QWR and in the QW regions the spatial PL variation in the low energy part of the emission is no longer limited to our spatial resolution. The luminescence originates from islands with an average extension of 400–600 nm in diameter as shown in Fig. 3, panels (a) and (c). For detection energies in the high-energy part of the emission bands, a completely different situation appears. Here a uniform PL distribution delocalized along the QWR axis [panel (b)] or over the squared scan region [panel (d)] reveals the existence of quasi-1D and -2D states for the QWR and the QW, respectively. Theoretical calculations of exciton states in a disordered quasi-1D and quasi-2D potential account well for such observed simultaneous coexistence of delocalized and localized excitonic states (for more details, see Refs. 17 and 26). Finally the image (e) shows the emission from the barrier. In this case by tuning the detection energy through the whole emission band we always found PL emission localized on big islands.

In order to summarize the optical properties of the sample and the different PL spatial distributions, we plot (Fig. 4) the PL intensity as a function of the detection energy and the

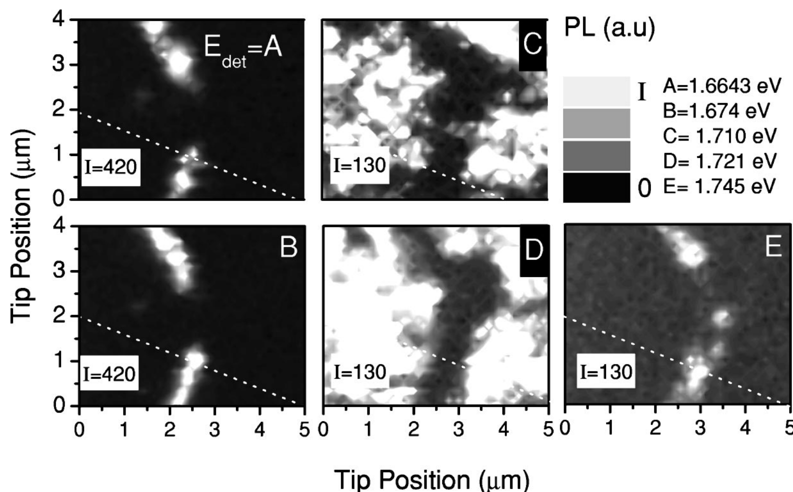

FIG. 3. Two-dimensional high-energy-resolution images taken at 10 K and at different detection energies $A=1.6643$ eV; $B=1.674$ eV; $C=1.710$ eV; $D=1.721$ eV; $E=1.745$ eV. The detection energies are indicated with the corresponding labels in the images and with arrows in the spectra of Figs. 2(a)–2(d).

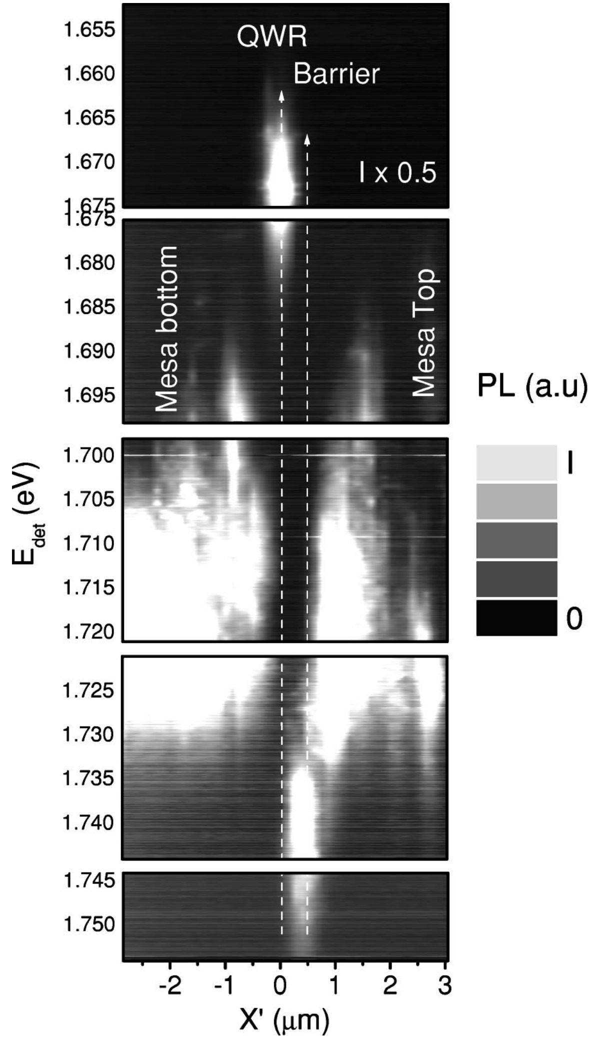

FIG. 4. Spatially resolved PL spectrum. The PL Intensity is plotted as a function of the detection energy E_{det} and of the lateral separation between the tip and the QWR located at $X'=0$.

lateral distance between the QWR, located at $X'=0$, and the fiber tip; the tip is moved perpendicular to the QWR axis, along the dashed line in Fig. 3.

The barrier region extends from 1.735 to 1.752 eV and its spatial distribution is peaked at $X'=0.5$ μm with a lateral extension of $\simeq$370 nm. The emission from the QW extends from 1.70 to 1.73 eV. The signal from the mesa top side is slightly blue shifted in respect to that from the bottom side. Finally the QWR emission extends from 1.665 to 1.685 eV and its lateral profile has a full width at half maximum of 150 nm (our resolution). Preliminary PLE experiments indicate that the lateral width of the confined region and the quasi-one-dimensional confinement energy of excitons are 70 nm and 55 meV, respectively. This corresponds to a splitting of about 7 meV between the two lowest electron subbands.

B. Potential energy profiles and growth mechanism

In this section we demonstrate that the precise and detailed information obtained from the near-field PL spectra

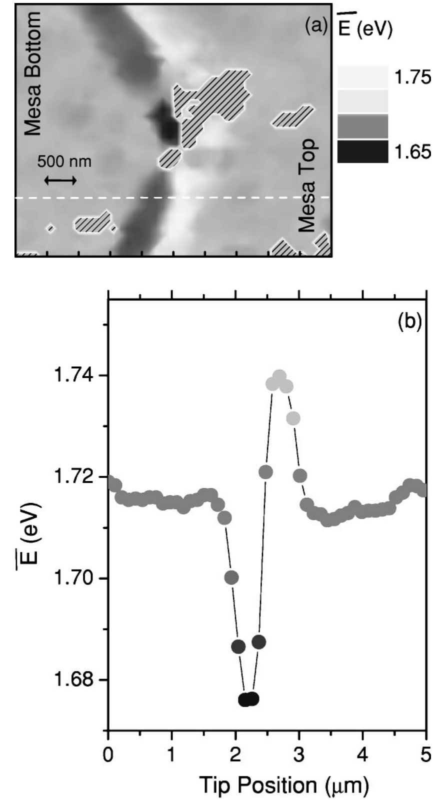

FIG. 5. (a) Two-dimensional map of the average energy emission $\bar{E}(x,y)$ [Eq. (1)]. (b) Cross section along the dashed line in Fig. 5(a).

allows to gain insight into the growth dynamics of this complex nanostructure. As already discussed in Ref. 23, the change in the local emission energy originates mainly from a change in the local thickness of the GaAs layer. The idea is then to first derive a 2D map of the average exciton emission energy and then to evaluate from such a map an estimate of two-dimensional variation of the local GaAs layer thickness.

The average emission energy $\bar{E}(x,y)$ is extracted by summing, at each position of the tip, all the emission energies weighted by the corresponding emission intensity

$$\bar{E}(x,y)=\frac{\sum_{E_i=1.61\ \mathrm{eV}}^{1.77\ \mathrm{eV}} I(x,y,E_i)E_i}{\sum_{E_i=1.61\ \mathrm{eV}}^{1.77\ \mathrm{eV}} I(x,y,E_i)}, \tag{1}$$

where $I(x,y,E_i)$ is the emission intensity at the position (x,y) and at the detection energy E_i which ranges from 1.61 to 1.77 eV at a step of 65 μeV.

The extracted 2D matrix is shown in Fig. 5(a). The patterned regions correspond to portions of the sample with a reduced luminescence yield ΣI of less than 10% of the maximum luminescence yield. The plot highlights the pronounced local decrease of $\bar{E}$ along the QWR axis, and—even more pronounced—at the dot position. It also evidences the high energy barrier region surrounding the zig-zag pattern on the mesa top side. The curve presented in Fig. 5(b) is a repre-

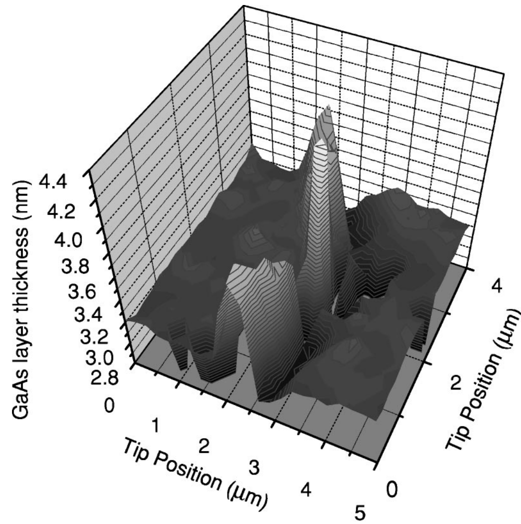

FIG. 6. 3D map of the GaAs layer thickness calculated from the average energy emission.

sentative cross section through the 2D image [dashed line in Fig. 5(a)]. On the mesa top the excitonic emission energy increases respect to the flat QW area by almost 24 meV over a length scale of about 500 nm as it approaches the QWR. On the contrary, on the mesa bottom the average emission from the QW is at 1.715 eV and there is no evidence for barrier formation.

Using this information and a ratio of 1.5:1 for the conduction–to–valence-band–offset energy in the 2D GaAs/AlGaAs structure, a 2D map of the GaAs layer thickness can be directly calculated in the effective-mass approximation with a finite-well model. The extra confinement arising from the further reduction in dimensionality in the wire and dot regions is neglected, therefore at these positions the extracted values for the GaAs layer thickness are slightly underestimated by less than 0.1 nm.

The results of this calculation are shown in Fig. 6. The flat QW area has an average thickness of 3.2 nm. As the QWR region is approached from the mesa top side, the average thickness goes down to 2.9 nm. This value corresponds to a decrease of about one monolayer with respect to the flat QW region. In the QWR region at the mesa sidewall the local thickness increases to $\simeq$3.8 nm. In the dotlike region at the intersection of two sidewalls the local GaAs layer thickness is $\simeq$4.4 nm. As already pointed out, no barrier and thus no further thinning is present on the mesa bottom side.

The thinning of the QW in proximity of the sidewall is a consequence of Ga adatom migration towards the sidewall during the growth process. This adatom migration gives rise to the formation of a thicker GaAs region at the edge (QWR formation) surrounded by thinner regions in the adjacent parts in the top and bottom areas.[18] In this structure we observe a reduction of the QW thickness only on the mesa top side of the sidewall. This indicates that, during the QW growth, migration of material occurs predominantly from the mesa top side and suggests that a strong asymmetry of the diffusion coefficient in the mesa top and bottom areas exists.

In order to clarify this point, we simulate the formation of the surface patterns during growth by using a simplified analytical continuum model. Both diffusion current driven by the spatial variation in the particle density and the drift current driven by the gradient of the chemical potential are included. Details of the simulations are given in the Appendix.

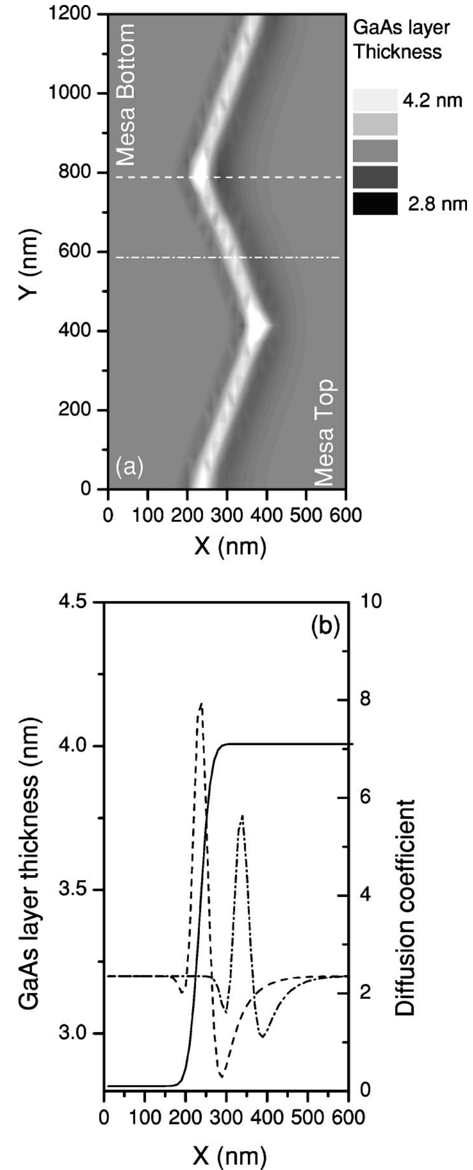

FIG. 7. (a) 2D GaAs layer profile, calculated with the analytical model presented in the Appendix. (b) Cross sections through Fig. 7; profile of the diffusion coefficient used in the calculation (solid line) in arbitrary units.

In Fig. 7(a) is plotted the 2D simulation of the sample thickness as obtained by solving Eq. (A5). Figure 7(b) shows the thickness profiles along the dashed and dot-dashed lines in Fig. 7(a). The increase of the GaAs layer at the sidewall and at the intersection of the sidewalls are visible. The asymmetric barrier formation is also evident. In our simulations, this asymmetric barrier formation arises only if we assume a strongly asymmetric diffusion coefficient, such as the one plotted in the same figure [Fig. 7(b)]. Assuming symmetric diffusion coefficients, the barriers are symmetric on both sides. The results of this simulation are equivalent for the

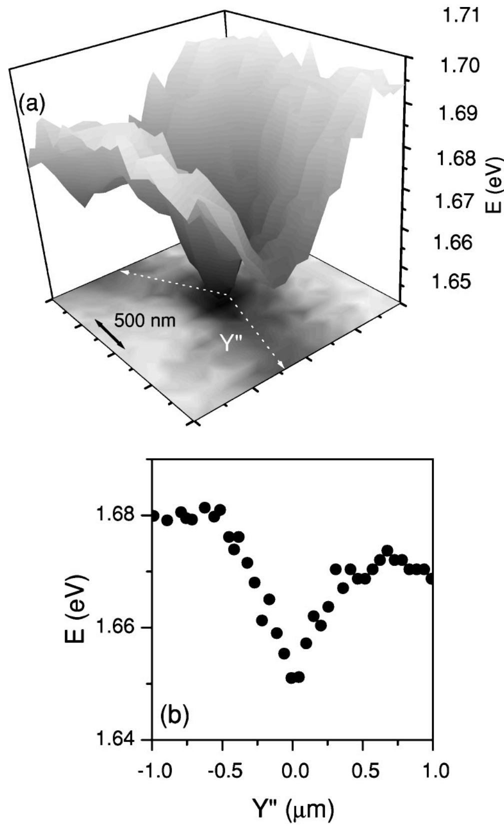

FIG. 8. (a) Detail of the average excitonic emission on a 2×2 μm^2 spot centered at the dot location. (b) Profile along the wire axis [dashed line in Fig. 8(a)].

two orientations (+ or −30°). In both cases we observe barrier formation on the top mesa side and dot formation at the corner. We can conclude that an asymmetric diffusion coefficient accounts for the asymmetric barrier formation, while probably, in order to reproduce the preferential formation of dotlike regions at the corner facing the top side, an additional difference in the surface tension for the two corners has to be included.

C. The wire-dot interface

As the height of the local barrier can strongly influence the carrier transport within the sample,[23] it is relevant to establish whether potential barrier exists at this interface to correctly interpret the results from the transport experiment illustrated in the next section. We therefore investigated a restricted region around the dot of 2×2 μm^2 with a pixel of 50 nm. Following the same procedure as for Fig. 5 we calculate the average emission energy in this restricted region. The result is plotted in Fig. 8(a). It is evident that, within our experimental accuracy, no barriers are detectable at the wire-dot interface. This becomes even clearer by looking at the curve of Fig. 8(b). Here the average energy is plotted along the coordinate Y″, which runs along the wire axis as indicated by the white arrows in Fig. 8(a). The results highlight that this novel nanostructure is highly suitable for optical studies of carrier transport along the single QWR, where the dot area is used as an optical marker for ambipolar diffusion via QW and QWR's states.

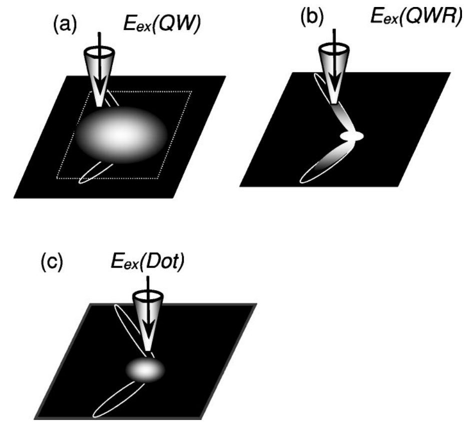

FIG. 9. (a)–(c) Schematic of the experimental configuration used for measuring diffusion in the QW and in the QWR. Images of the dot emission are taken at three excitation energies $E_{\rm ex}$(QW), $E_{\rm ex}$(QWR), $E_{\rm ex}$(dot): carriers are created resonantly with the QW the QWR and the dot, respectively.

IV. RESULTS: NEAR−FIELD−OPTICAL TRANSPORT MEASUREMENTS

To gain insight into the transport properties of the QWR, we record near-field PLE images of the dot area. The near-field microscope is now used in the collection geometry: the laser beam is coupled into the fiber and the PL signal is collected in far field through a conventional microscope objective. A metal-coated aperture probe is used in these experiments. The detection energy is fixed at the dot emission (1.64 eV) and the excitation energy is varied. The tip is scanned over an area of 5.4×5.4 μm^2 centered at the dot position. Images of the dot emission are taken at three excitation energies $E_{\rm ex}$(QW), $E_{\rm ex}$(QWR), $E_{\rm ex}$(dot), selected in order to create carriers resonantly to the lowest QW, QWR, and dot transitions. Figures 9(a)–9(c) illustrate the three different situations: First by tuning the excitation energy resonant with the QW, carriers are created in the entire area covered by the tip scan range. The occurrence of dot luminescence after QW excitation involves carrier diffusion and trapping, i.e., a collection of carriers into the dot. PL images recorded at the dot emission energy are thus expected to have approximately a circular shape, centered at the dot location, with a diameter proportional to the carriers diffusion length in the well. In the second configuration [Fig. 9(b)] carriers are created resonantly with the wire, the spatial distribution of the dot PL signal is now expected to be elongated through the two QWR branches with a length proportional to the QWR diffusion length. Finally, for excitation resonant with the dot, the PL image is expected to reproduce the dot shape convoluted with the spatial resolution of the experiment Fig. 9(c).

Figures 10(a) and 10(b), show the experimental data obtained at 10 and 80 K, respectively. At low temperature [Fig. 10(a)], independent of the excitation energy, the images

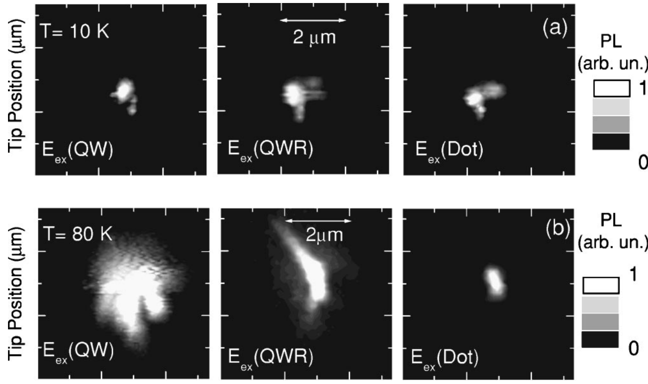

FIG. 10. Two-dimensional NSOM images recorded with a etched coated tip at (a) 10 K and (b) 80 K; the excitation energies E_{ex}(QW), E_{ex}(QWR), E_{ex}(dot) are selected in order to create carriers resonantly with QW, QWR, and dot; the detection energy is tuned at the dot PL peak.

show the PL spatially located on a narrow region around the dot. At 80 K, however, a different situation appears [Fig. 10(b)]. Depending on the excitation energy, the PL spatial distribution is strongly modified. It has a circular shape in the case of the QW excitation and reveals broad tails that extend exponentially into the wire region in the case of QWR excitation. Finally for excitation resonant with the dot we find the image of the dot broadened by the spatial resolution.

In Figs. 11(a) and 11(b), the spatial profiles of the PL at 80 K are extracted by the images reported in Fig. 10(b). The intensity of the PL is plotted (dots) versus the distance between the tip and the dot (X), when the tip is moved within the embedding QW [Fig. 11(a)] and along the QWR, respectively [Fig. 11(b)]. In both figures the PL intensity profile for E_{ex}(dot) (dashed lines) show the broadening of the resolution.

In a steady-state diffusion model,[27] the PL signal $I_{dot}(x)$ is expected to decrease exponentially with increasing distance from the dot:

$$I_{dot}(x) \propto \exp(-|X|/L), \tag{2}$$

where L is the diffusion length and X the distance between the tip and the dot. The data in Figs. 11(a) and 11(b) exhibit this behavior. Values of $L_{QW}=650\pm100$ nm and $L_{QWR}=600\pm100$ nm are derived for the QW and QWR diffusion length, respectively. From the low temperature data, where the spatial profile of the dot PL is limited by the spatial resolution, we extract for the diffusion lengths L_{QW} and L_{QWR} an upper limit of 120 nm.

From the observed diffusion lengths and the lifetime $\tau_{QW}=1.3$ ns and $\tau_{QWR}=1.5$ ns, measured in a similar structure,[12] one can estimate the 2D and 1D diffusion coefficients $D_{QW}=L_{QW}^2/\tau$, $D_{QWR}=L_{QWR}^2/(2\tau)$ and the corresponding mobility μ_{QW} and μ_{QWR} once the Einstein relation $\mu=eD/k_BT$ is applied. The results are shown in Table I. The value found for the 2D mobility μ_{QW} is in good agreement with the value reported in literature[28] for excitonic mobility in QW's of similar thickness.

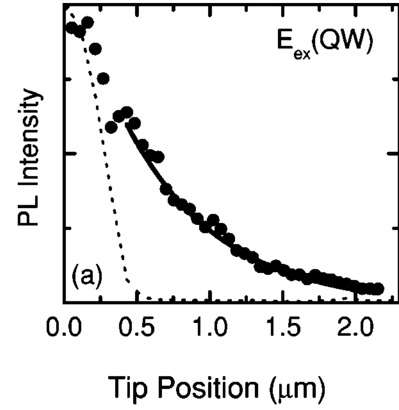

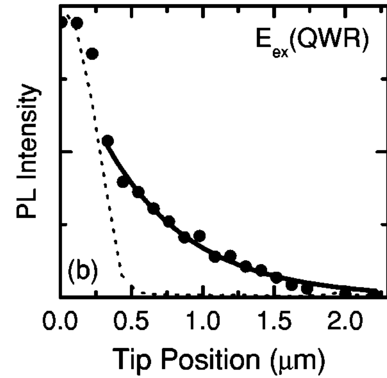

FIG. 11. Spatial profile of the dot luminescence at 80 K. (a) Excitation energy E_{ex}(QW), tip moved in the QW region. (b) Excitation energy E_{ex}(QWR), tip moved along the QWR axis. Dashed lines: spatial resolution.

It has been shown that the experimentally observed 2D exciton mobility can be well described by the inclusion of three mechanisms: scattering by ionized impurities, scattering by acoustic phonons via the deformation potential and polar-optical scattering. For small well widths (≤ 8 nm) the barrier-alloy scattering and the interface roughness scattering have to be included also.[28,29]

Each of these scattering processes has a different temperature dependence. Scattering by acoustic phonons and polar-optical scattering are expected to dominate at temperatures higher than 100 K and to determine a decrease of the exciton mobility with the rising of the temperature. The alloy scat-

TABLE I. Exciton diffusion coefficients and mobilities obtained from the profiles of Fig. 11 and fits of Eq. (2).

	$T=10$ K	$T=80$ K
D_{QW}	≤ 0.1 cm^2/s	3 cm^2/s
D_{QWR}	≤ 0.05 cm^2/s	1.2 cm^2/s
μ_{QW}	≤ 115 cm^2/V s	435 cm^2/V s
μ_{QWR}	≤ 60 cm^2/V s	174 cm^2/V s

tering is expected to be temperature independent and yields an upper limit for the mobility in the temperature range between 70 and 150 K. Finally the interface roughness scattering dominates in the low temperature range (10–100 K) and give rise to an increase of the mobility with the rising of the temperature. As a matter of fact it has been shown that a mobility dependence on the temperature in this range is a clear signature of the interface quality: For smooth interface the low temperature mobility is almost temperature independent.[29]

For QWR structures in the extreme quantum limit (EQL), the one dimensional character of the electrons and exciton motion is expected to give rise to a reduction in the scattering processes,[30–32] with a consequent drastic increase of the mobility. Nevertheless, when the wire width is reduced, the interface roughness scattering is expected to become increasingly important[33] and the estimated values for the mobility approach the 2D ones.

From the values reported in Table I, two main aspects are evident, first the similarity between the 2D and the 1D diffusion coefficient and second the strong dependence, in both cases, on the temperature: the measured diffusion coefficient at 80 K is more that 30 times higher than the corresponding low temperature one. We conclude that in both cases, mobilities are dominated by interface scattering.

V. CONCLUSION

We have presented low temperature near field spectroscopic experiments on a novel coupled wire-dot structure. High spectral- and spatial-resolution PL provides evidence of both excitons localized at local potential minima of the structure and in delocalized quasi-one-dimensional states. PL images at different detection energies reveal the existence of distinct regions of the structure with characteristic spatial and quantum-mechanical features. An analysis of the near field optical images gives potential energy profiles of the structure. A potential barrier originating from local thinning of the GaAs layer by about 1 ML at the well-wire interface on the mesa top side has been detected. This indicates that during the growth process, migration of material occurs predominantly from the mesa top side. These results are well simulated by using a drift-diffusive model with the inclusion of an asymmetric diffusion coefficient.

We have presented a method for studying transport in single QWRs where the dot area is used as an optical marker for excitonic diffusion via QW and QWR states. This method allows one to measure under the same experimental conditions both 2D and 1D diffusion coefficients. The measured values for the diffusion coefficient and their dependence on the temperature suggest that in both the QW and QWR regions scattering by interface roughness dominates the transport properties.

ACKNOWLEDGMENTS

This work was supported by the Deutsche Forschungsgemeinschaft (SFB296) and the European Union through the EFRE program. One of the authors (V.E.) gratefully acknowledges the TMR program for financial support under Proposal No. ERB4001GT975127.

APPENDIX

The growth of low-dimensional nanostructures on patterned surfaces relies on the interplay between adatom surface diffusion and local variations in the surface chemical potential μ. The growth rates dz/dt are assumed to follow a standard drift-diffusion equation $dz/dt=-\Omega_0\vec{\nabla}\vec{j}+G-z/\tau$, where Ω_0 is the atomic volume, j is the particle current, R is the local growth rate in the absence of adatom drift-diffusion, and τ the lifetime of the diffusing adatoms: The incident atoms either diffuse to adjacent sites or get incorporated with a rate $R=n/\tau$ (n=particle density). The particle current is composed by two terms, a drift-current $j_{\mathrm{dr}}=-n\nu\nabla\mu$,[34] driven by the gradient in the chemical potential ($\nu=eD/kT$, where k is the Boltzman constant and T the growth temperature) and a diffusion current $j_d=-D\nabla n$,[35] driven by the spatial variation in the particle density.

In one spatial dimension, ξ, variations in the surface chemical potential μ of the component i of an alloy at the growth temperature T may be written as[34]

$$\mu_i=\mu_0+[\sigma_\tau(\xi)]^2/2E+[\gamma(\theta)+\gamma''\theta)]\kappa(\xi)+\frac{kT}{\Omega_0}\ln x_i(\xi). \tag{A1}$$

Here σ_τ is the tangential surface stress, E the elastic modulus,[36] and x_i the mole fraction.

For self-ordering of lattice-matched strain-free structures, the dominant term is the third one, which is related to the surface curvature κ and involves the (orientation-dependent) surface free energy.[37] The second and the fourth one related, respectively, to the surface stress and the entropy-of-mixing, can be neglected.[34]

For the structures formed at the sidewall of patterned GaAs (311)A substrates, the curvature-related contribution to μ can be expressed by

$$\mu-\mu_0\propto-\exp[-(x-xc)^2/\sigma^2]. \tag{A2}$$

Here xc denotes the center of the sidewall and σ is related to the sidewall width.

According to this model, the self-limited thickness profile of a one-dimensional quantum wire structure is given by the steady-state solution ($dz/dt=0$) of

$$dz/dt=0=D\frac{\partial^2 z}{\partial x^2}+\frac{\partial D}{\partial x}\frac{\partial z}{\partial x}+z\nu\frac{\partial^2\mu}{\partial x^2}+\nu\frac{\partial\mu}{\partial x}\frac{\partial z}{\partial x}+z\frac{\partial\nu}{\partial x}\frac{\partial\mu}{\partial x}+G-z/\tau. \tag{A3}$$

In the case of the growth zig-zag-patterned substrates we introduce the two-dimensional surface mobility:

$$\mu=\mu_0\exp\{-[x-xs(y)]^2/\sigma^2\}\}\mu_1\exp[-(y-yc)^2/\sigma^2+1]. \tag{A4}$$

This assumption is justified by the prediction that the "growth selectivity" increases at the sidewall intersection (i.e., there is a local minimum in μ). We therefore keep for μ the same Gaussian dependence along x as in the 1D case and we assume a Gaussian-shaped decrease in μ at the intersection of the two sidewalls [the sidewalls are oriented under $+$ or $-30°$ with respect to the x direction; $xc(y)$ follows the shape of the zig-zag pattern].

Therefore Eq. (A3) transforms into

$$dz/dt=0=D\frac{\partial^2 z}{\partial x^2}+\frac{\partial D}{\partial x}\frac{\partial z}{\partial x}+z\nu\frac{\partial^2\mu}{\partial x^2}+\nu\frac{\partial\mu}{\partial x}\frac{\partial z}{\partial x}+z\frac{\partial\nu}{\partial x}\frac{\partial\mu}{\partial x}+D\frac{\partial^2 z}{\partial y^2}+\frac{\partial D}{\partial y}\frac{\partial z}{\partial y}+z\nu\frac{\partial^2\mu}{\partial y^2}+\nu\frac{\partial\mu}{\partial y}\frac{\partial z}{\partial y}+z\frac{\partial\nu}{\partial y}\frac{\partial\mu}{\partial y}+G-z/\tau. \tag{A5}$$

*Present address: LENS (Laboratorio Europeo di Spettroscopie non Lineari), I-50125 Firenze, Italy. emiliani@fi.infn.it

[1] For a recent review see: Ch. Lienau and T. Elsaesser, in *Semiconductors and Semimetals*, edited by K. T. Tseng (Academic Press, New York, 2001), Vol. 67, p. 39.
[2] R. D. Grober, T. D. Harris, J. K. Trautman, E. Betzig, W. Wegscheider, L. Pfeiffer, and K. W. West, Appl. Phys. Lett. **64**, 1421 (1994).
[3] T. D. Harris, D. Gershoni, R. D. Grober, L. Pfeiffer, K. West, and N. Chand, Appl. Phys. Lett. **68**, 988 (1996).
[4] A. Richter, G. Behme, M. Süpitz, Ch. Lienau, T. Elsaesser, M. Ramsteiner, R. Nötzel, and K. H. Ploog, Phys. Rev. Lett. **79**, 2145 (1997).
[5] J. Hasen, L. N. Pfeiffer, A. Pinczuk, S. He, K. W. West, and B. S. Dennis, Nature (London) **390**, 54 (1997).
[6] J. Bellessa, V. Voliotis, R. Grousson, X. L. Wang, M. Ogura, and H. Matsuhata, Appl. Phys. Lett. **71**, 2481 (1997).
[7] For a recent review see: A. Zrenner, J. Chem. Phys. **112**, 7790 (2000).
[8] K. Brunner, U. Bocklemann, G. Abstraiter, M. Walther, G. Böhm, G. Tränkle, and G. Weimann, Phys. Rev. Lett. **69**, 3216 (1992).
[9] H. F. Hess, E. Betzig, T. D. Harris, L. N. Pfeiffer, and K. W. West, Science **264**, 1740 (1994).
[10] D. Gammon, E. S. Snow, and D. S. Katzer, Appl. Phys. Lett. **67**, 2391 (1995).
[11] Y. Toda, O. Moriwaki, M. Nishioka, and Y. Arakawa, Phys. Rev. Lett. **82**, 4114 (1999).
[12] A. Richter, M. Süptitz, D. Heinrich, Ch. Lienau, T. Elsaesser, M. Ramsteiner, R. Nötzel, and K. H. Ploog, Appl. Phys. Lett. **73**, 2176 (1998).
[13] T. Guenther, V. Emiliani, F. Intonti, Ch. Lienau, T. Elsaesser, R. Notzel, and K. H. Ploog, Appl. Phys. Lett. **75**, 3500 (1999).
[14] M. Achermann, B. A. Nechay, U. Siegner, A. Harmann, D. Oberli, E. Kapon, U. Keller, Appl. Phys. Lett. **76**, 2695 (2000).
[15] V. Emiliani, T. Guenther, Ch. Lienau, T. Elsaesser, R. Nötzel, and K. H. Ploog, Phys. Rev. B **61**, R10 583 (2000).
[16] Y. Toda, T. Sugimoto, M. Nishioka, and Y. Arakawa, Appl. Phys. Lett. **76**, 3887 (2000).
[17] F. Intonti, V. Emiliani, Ch. Lienau, T. Elsaesser, R. Nötzel, and K. H- Ploog, Phys. Rev. B **63**, 075313 (2001).
[18] R. Nötzel, M. Ramsteiner, J. Menniger, A. Trampert, H.-P. Schönherr, L. Däweritz, and K. -H. Ploog, Jpn. J. Appl. Phys., Part 2 **35**, L297 (1996).
[19] J. Fricke, R. Nötzel, U. Jahn, H.-P. Schönherr, L. Däweritz, and K. H. Ploog, J. Appl. Phys. **85**, 3576 (1999).
[20] J. Fricke, R. Nötzel, U. Jahn, H.-P. Schönherr, M. Ramsteiner, and K. H. Ploog, J. Appl. Phys. **86**, 2896 (1999).
[21] G. Behme, A. Richter, M. Süptitz, and Ch. Lienau, Rev. Sci. Instrum. **68**, 3458 (1997).
[22] P. Lambelet, A. Sayah, M. Pfeffer, C. Philipona, and F. Marquis-Weible, Appl. Opt. **37**, 7289 (1998).
[23] Ch. Lienau, A. Richter, G. Behme, M. Süptitz, D. Heinrich, T. Elsaesser, M. Ramsteiner, R. Nötzel, and K. H. Ploog, Phys. Rev. B **58**, 2045 (1998).
[24] F. Intonti, V. Emiliani, Ch. Lienau, T. Elsaesser, V. Savona, E. Runge, and R. Zimmermann, Phys. Rev. Lett. **87**, 076801 (2001).
[25] H. Castella, and J. W. Wilkins, Phys. Rev. B **58**, 16 186 (1998).
[26] O. Di Stefano, S. Savastava, G. Martino, and R. Girlanda, Appl. Phys. Lett. **77**, 2804 (2000).
[27] The observation of excitonic recombination in the dot requires that both electrons and holes reach the dot region. Under the present experimental condition we are thus sensitive to diffusive transport of electron-hole pairs.
[28] H. Hillmer, A. Forchel, S. Hansmann, M. Morohashi, E. Lopez, H. P. Meier, and K. H. Ploog, Phys. Rev. B **39**, 10 901 (1989).
[29] H. Hillmer, A. Forchel, R. Sauer, and C. W. Tu, Phys. Rev. B **42**, 3220 (1990).
[30] H. Sakaki, Jpn. J. Appl. Phys., Part 2 **19**, L735 (1980).
[31] G. Fasol, Appl. Phys. Lett. **61**, 831 (1992).
[32] M. Oestreich, W. Rühle, H. Lage, D. Heitmann, and K. Ploog, Phys. Rev. Lett. **70**, 1682 (1993).
[33] J. Motohisa and H. Sakaki, Appl. Phys. Lett. **60**, 1315 (1992).
[34] G. Biasiol and E. Kapon, Phys. Rev. Lett. **81**, 2962 (1998).
[35] A. Hartmann, L. Vescan, S. Dieker, and H. Lüth, J. Appl. Phys. **77**, 1959 (1995).
[36] Q. Xie, A. Madhukar, P. Chen, and N. P. Kobayashi, Phys. Rev. Lett. **75**, 2542 (1995).
[37] C. Herring, in *The Physics of Powder Metallurgy*, edited by W. E. Kingston (McGraw-Hill, New York, 1951).